12^{th} International Conference on Fracture Mechanics of Concrete and Concrete Structures
FraMCoS-12
B.L.A. Pichler, Ch. Hellmich, P. Preinstorfer (Eds)

https://doi.org/10.21012/FC12.1300
MS10-1:5

TWO-WAY COUPLED MULTIPHYSICS SIMULATION OF LATTICE DISCRETE PARTICLE MODEL

GIANLUCA CUSATIS[*], HAO YIN[*] MATTHEW TROEMNER[†], WEIXIN LI[*], EROL LALE[*], LIFU YANG[‡], LEI SHEN[^], MOHAMMED ALNAGGAR[±] AND GIOVANNI DI LUZIO[∓]

[*] Northwestern University, Civil and Environ. Eng.
Evanston, 60208, IL, USA
e-mail: g-cusatis@northwestern.edu

[†]North Fracture Group
Houghton, MI 49931, USA
e-mail: congress@framcos.org, www.framcos.org

[‡]City University of Hong Kong, Department of Architecture and Civil Eng.
Hong Kong, 999077, China
e-mail: congress@framcos.org, www.framcos.org

[^]Hohai University, College of Water Conservancy and Hydropower Eng.
Nanjing, 210098, China
e-mail: congress@framcos.org, www.framcos.org

[±]Oak Ridge National Laboratory
Oak Ridge, TN 37830, USA

[∓]Politecnico di Milano, Department of Civil and Environ. Eng.
Milan, 20133, Italy
e-mail: giovanni.diluzio@polimi.it

Key words: Two-way coupling, Interprocess communication, Hydro-mechanical coupling, Lattice discrete particle, Dual lattice

Abstract. In this study, a Multiphysics-Lattice Discrete Particle Model (M-LDPM) framework that deals with coupled-fracture-poroflow problems has been introduced. The M-LDPM framework uses two lattice systems, the LDPM tessellation and the Flow Lattice Element (FLE) network, to represent the heterogeneous internal structure of typical quasi-brittle materials like concrete and rocks, and to simulate the material's mechanical behavior and mass transport at the coarse aggregate scale. In this study, the LDPM governing equations are revisited and modified to include the influence of fluid pore pressure. The governing equations of the Flow Lattice Model (FLM) for pore pressure flow are derived using mass conservation balances for both uncracked and cracked specimens. The proposed M-LDPM framework was implemented using Abaqus user element subroutine VUEL for mechanical behavior within the explicit dynamic procedure and user subroutine UEL for mass transport within the implicit transient procedure. The coupling of the two models was achieved using Interprocess Communication (IPC) between Abaqus solvers. The M-LDPM framework can simulate the variation of permeability induced by fracturing processes by relating the transport properties of flow elements with local cracking behaviors. The proposed model is validated by comparing the numerical results with analytical solutions of classical benchmarks found in poromechanics literature.

1 INTRODUCTION

The durability of materials used in constructing buildings and infrastructure is governed by a complex interaction between their mechanical properties and multiphysical behaviors. While structural design primarily focuses on meeting strength and safety criteria, long-term performance often deviates from initial predictions, leading to unforeseen maintenance costs and reduced service life. This highlights the importance of integrating durability considerations into design principles, accounting for factors such as environmental conditions, material degradation, and load-induced wear. It is crucial to incorporate the various factors affecting material durability into design principles to produce a structure with an optimal lifespan and to minimize their environmental footprint.

The interaction between fracture, mass transport, and heat transfer is a well-studied multiphysics phenomenon with significant implications for material behavior. Experimental studies have demonstrated that fracture permeability is governed by a complex interplay of physical processes and is influenced by factors such as crack openings and roughness [1, 2, 3], chemical precipitation and dissolution[4, 5], and thermal effects [6]. Among these, the presence of open and interconnected crack patterns plays a particularly critical role in determining permeability. Extensive research highlights that fracture permeability is strongly correlated with the density, spacing, orientation, width, and length of cracks within a material, emphasizing the importance of understanding these parameters in the analysis and prediction of transport properties in fractured systems [7, 8, 9].

This work develops a numerical framework called the Multiphysics Lattice Discrete Particle Model (M-LDPM) to study the two-way coupling behavior of porous flow and fracture permeability of quasi-brittle materials in three-dimensional (3D) simulations. The M-LDPM framework has been verified by simulating various classical benchmark examples, including 1D Terzaghi's consolidation and hydraulic fracturing.

2 LATTICE DISCRETE PARTICLE MODEL (LDPM) FOR MULTI-PHYSICS ANALYSES

The dual graph approaches have been widely adopted in subjects such as physics, chemical engineering, biological engineering, and material sciences in the past several decades [10, 11, 12, 13, 14, 15, 16]. In the field of poromechanics, Grassl [17] introduced the concept of dual lattice, incorporating aligned cracks and conduit elements to effectively capture the impact of crack openings on fluid flow. This approach was subsequently extended to three-dimensional analyses [18] and has been applied in numerous studies. For instance, it has been used to simulate cracking caused by rebar corrosion [19] and hydraulic fracturing processes [20, 21, 22]. Li et al. [23] expanded the dual lattice framework to model shale fractures, incorporating the effects of mechanical volumetric strain rates on pressure. Similarly, Shen et al. [24, 25] employed the approach to accurately simulate thermal spalling and thermal strains in concrete under multiaxial loads at high temperatures. Yang et al. [26, 27] further applied the dual lattice concept to model volumetric strain and cracking in concrete induced by alkali-silica reactions. These studies demonstrate the versatility and effectiveness of the dual lattice framework in capturing complex multiphysical phenomena in fractured systems.

A typical usage of topologically dual lattice systems is the Multiphysics-Lattice Discrete Particle Model (M-LDPM) for the multiscale multiphysics analysis of granular-dominant quasibrittle materials (e.g., concrete, rock). M-LDPM is formulated in a discrete poromechanics setting by adopting two coupled dual lattices simulating mechanical and transport behaviors, respectively. The model adopts an a priori discretization of the internal structure of the material at the mesoscale, which is the length scale of major material heterogeneities.

2.1 Governing equations

2.1.1 LDPM Kinematics and Constitutive Laws

In the LDPM formulation, adjacent polyhedral cells interact through shared triangular facets. Three strain measures, one normal component and two shear components, are defined using displacement jump, $[\![\mathbf{u}_C]\!]$, at each facet center as:

$$e_N = \frac{1}{\ell}\mathbf{n}^{\mathrm{T}}\cdot[\![\mathbf{u}_C]\!];\; e_M = \frac{1}{\ell}\mathbf{m}^{\mathrm{T}}\cdot[\![\mathbf{u}_C]\!];\; e_B = \frac{1}{\ell}\mathbf{b}^{\mathrm{T}}\cdot[\![\mathbf{u}_C]\!] \tag{1}$$

where ℓ = tetrahedron edge length associated with the facet; $\mathbf{n}$ is a unit vector normal to each facet, and $\mathbf{m}$ and $\mathbf{b}$ are two mutually orthogonal unit vectors orthogonal to $\mathbf{n}$. The facet stress vector applied to the solid phase, $\mathbf{t} = t_N\mathbf{n} + t_M\mathbf{m} + t_B\mathbf{b}$, is calculated through appropriate constitutive laws, for more details see [28, 29, 30] .

In the elastic regime, the mechanical facet stress components are proportional to the corresponding strain components:

$$\mathbf{t} = \begin{bmatrix} t_N \\ t_M \\ t_B \end{bmatrix} = \begin{bmatrix} E_N & 0 & 0 \\ 0 & E_M & 0 \\ 0 & 0 & E_B \end{bmatrix} \begin{bmatrix} e_N \\ e_M \\ e_B \end{bmatrix} \tag{2}$$

where $E_N = E_0$ is the normal modulus, $E_M = E_B = \alpha E_0$ is the shear modulus, and α = normal-shear coupling coefficient.

Beyond the elastic limit, the constitutive law is designed to capture three distinct nonlinear behaviors that govern material response. The first source of nonlinearity arises from fracturing and cohesive behavior under tensile conditions, characterized by positive normal strain ($e_N > 0$). The second nonlinear phenomenon is associated with pore collapse and material compaction, occurring under compressive conditions ($e_N < 0$). Lastly, frictional behavior under compression introduces another source of nonlinearity, which is effectively modeled using a non associative incremental plasticity.

The facet stresses calculated through the constitutive laws represent the stresses carried by the solid phase. Equilibrium considerations at the facet level allow for the reasonable assumption of a parallel coupling between the stresses carried by the solid phase and those by the fluid phase. In this work, the effective stress concept from Biot's theory of poroelasticity [31] is adopted, and the total stress vector on each facet is computed as

$$\mathbf{t}^{\mathrm{total}} = \mathbf{t} - b\mathbf{t}^{\mathrm{eigen}} \tag{3}$$

where b is the Biot coefficient, and $\mathbf{t}^{\mathrm{eigen}} = p\mathbf{n}$, p is the magnitude of effective pore pressure of fluid. The negative sign in Eq. 3 comes from the pressure sign convention, which is positive for the fluid and negative for the solid.

The equilibrium is obtained through the linear and angular momentum balance equations of each polyhedral cell, as follows:

$$\sum_{k\in\mathcal{F}_I} A_k\mathbf{t}_k^{\mathrm{total}} + V^I\mathbf{b} = \mathbf{M}_u^I\ddot{\mathbf{u}}_I + \mathbf{M}_\varphi^I\ddot{\boldsymbol{\varphi}}_I \tag{4}$$

$$\sum_{k\in\mathcal{F}_I} A_k\mathbf{c}_k^I \times \mathbf{t}_k^{\mathrm{total}} + V^I\mathbf{a}^I \times \mathbf{b} = \mathbf{I}_u^I\ddot{\mathbf{u}}_I + \mathbf{I}_\varphi^I\ddot{\boldsymbol{\varphi}}_I \tag{5}$$

where $\mathcal{F}_I$ is the set of facets surrounding the node P_I (located inside cell I); A_k is the projected area of k-th facet orthogonal to the corresponding tetrahedron edge, V^I is the cell volume, $\mathbf{c}_k^I$ is the distance between facet centroid and particle center, $\mathbf{a}^I$ is the distance between the cell centroid and the particle center, $\mathbf{b}^I$ is the external body force, $\mathbf{t}_k$ is the stress traction vector, $\mathbf{M}_i^I$ and $\mathbf{I}_i^I$ ($i = u, \varphi$) are inertia matrices, and $\mathbf{u}_I$ and $\boldsymbol{\varphi}_I$ are displacement and rotation vectors, respectively. In the current implementation, an explicit dynamic algorithm is adopted to solve the equations above by a quasi-static method.

2.1.2 Discrete Formulation of Fluid Flow

Following Li et al. [23], Flow Lattice Element (FLE) is formulated under the assumption of full saturation, constant ambient temperature, considering slightly compressible Newtonian fluid. According to the settings depicted in [32], each FLE connects the centroids

of two adjacent LDPM tetrahedra in the undeformed configuration: named tet $P_1P_2P_3P_4$ and tet $P_1P_2P_3P_5$ (Fig. 1 a). The two adjacent LDPM tetrahedra have a common triangular face A_0 with a normal $\mathbf{n}$, across which an FLE connects the tetpoints N_1 and N_2 located inside the two tetrahedra. A directional vector $\mathbf{e}$ orienting from N_1 to N_2 represents the flow direction in the FLE. The FLE is associated to two pyramidal volumes, V_1 and V_2, identified by the points P_1, P_2, P_3, N_1 and P_1, P_2, P_3, N_2. The volumes can be computed as $V_i = Al_i/3$ $(i = 1, 2)$, where $A = |\mathbf{n} \cdot \mathbf{e}|A_0$ is the projected area of triangular cross-section $P_1P_2P_3$ (A_0) in the direction $\mathbf{e}$; the segment lengths l_i are associated with the total length of FLE l, which intersects the cross-section $P_1P_2P_3$ (A_0), one can define the length proportionality coefficients which satisfy the relations $g_i = l_i/l$ $(i = 1, 2)$.

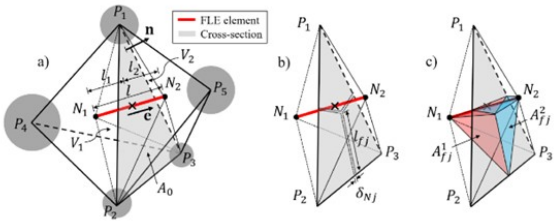

Figure 1: Diagrams of the Flow lattice element (FLE): a) FLE geometry, b) the associated LDPM facets; c) the cracked triangle face and the illustration of normal crack opening.

Fluid Flux for Uncracked Material

The mass of fluid in the uncracked control volume V_i $(i = 1, 2)$ can be written as $M^i_{fu} = m_{fi}V_i$ in which m_{fi} is the fluid mass content, defined to be the fluid mass per unit reference volume. The change in fluid mass content can be related to the increment of fluid content $\zeta_i = (m_{fi} - m_{f0})/\rho_{f0}$, where m_{f0} and ρ_{f0} are fluid mass content and density in the reference state, respectively. For slightly compressible fluids, the fluid density in the current state can be related to ρ_{f0} by defining the bulk modulus K_f; one can write $\rho_{fi} = \rho_{f0}\,[1 + (p_i - p_0)/K_f]$ $(i = 1, 2)$, where p_i is the current fluid pressure in V_i, and p_0 is the initial/reference pressure.

According to the classic theory of poromechanics [31, 33], the increment of fluid content, ζ_i, can be expressed as a linear combination of the volumetric strain, e_{vi}, of the solid phase defined as the relative variation of the solid volume, and the fluid pressure, p_i, as $\zeta_i = be_{vi} + p_i/M_b$, where M_b denotes the Biot modulus. It is worth pointing out that b and M_b may vary due to material heterogeneity. The effect of this variation is insignificant in the context of this paper and will be neglected thereinafter.

One can write the time variation of the fluid mass in the control volume V_i $(i = 1, 2)$ as:

$$\dot{M}^i_{fu} = \rho_{f0}\left(b\dot{e}_{vi} + \frac{\dot{p}_i}{M_b}\right)V_i \tag{6}$$

The mass flux through the uncracked area A from V_1 into V_2 reads $Q_{fu} = Aj_p$, the flux density j_p can be obtained by using Darcy's law, which can be written as:

$$j_p = -\bar{\rho}_f \frac{\kappa_0}{\mu_f} g_p \tag{7}$$

where κ_0 and μ_f denote the intrinsic permeability of the material and the fluid viscosity, respectively, $\bar{\rho}_f = g_2\rho_{f1} + g_1\rho_{f2}$ is an estimate of the weighted average density of fluid in the volume V, and g_p is the discrete estimation of pore pressure gradient from V_1 into V_2.

Fluid Flux for Cracked Material

The influence of cracks on the FLE can be considered in two parts: (1) the fluid mass stored in the cracked volumes, and (2) the fluid flux through the cracked surfaces. The fluid mass stored in the cracks is $M^i_{fc} = \rho_{fi}V_{ci}$, where the cracked volume can be expressed as $V_{ci} = \sum_{j=1}^{3} A^i_{fj}\delta^i_{Nj}$, A^i_{fj} are the areas of six LDPM facets associated with the FLE A^i_{f1}, A^i_{f2}, and A^i_{f3} belonging to V_i $(i = 1, 2)$, and δ^i_{Nj} are the normal crack openings, as shown in Fig. 1b and c.

The time variation of the fluid mass in the cracks can be written as:

$$\dot{M}^i_{fc} = \rho_{f0}\frac{V_{ci}}{K_f}\dot{p}_i + \rho_{fi}\dot{V}_{ci} \tag{8}$$

The fluid mass flux, Q_{fc}, from V_1 into V_2 associated with the cracks, can be approximated

by assuming a steady laminar flow between two crack surfaces with a cross section of length l_{fj} and width δ^i_{Nj} with $j = 1, 2, 3$, where l_{fj} represents the intersection of the j th facet with the tetrahedron face A (Fig. 1b). In this case, the solution of a two-dimensional Poiseuille flow in a channel, known as Poiseuille's formula, can be adopted [34]. One can write

$$Q_{fc} = \bar{\rho}_f \frac{\kappa_c}{\mu_f} A \frac{p_1 - p_2}{l} \tag{9}$$

where

$$\kappa_c = \frac{1}{12A} \left(\frac{g_2}{I_{c1}} + \frac{g_1}{I_{c2}} \right)^{-1} \tag{10}$$

and $I_{ci} = \sum_{j=1}^{3} l_{fj} \left(\delta^i_{Nj}\right)^3$ $(i = 1, 2)$. Connection in series of the cracked permeabilities in V_{c1} and V_{c2} is assumed for deriving Eq. 10.

The total fluid mass and total fluid flux can be obtained by adding the contributions from the uncracked and cracked domains. By collecting all terms introduced above and normalized both left and right hand sides with the reference fluid density ρ_{f0}, the mass balance equations for volume V_1 and V_2 can be written as:

$$\begin{aligned} &\left(b\dot{e}_{v1} + \frac{\dot{p}_1}{M_b} \right) V_1 + \frac{V_{c1}\dot{p}_1}{K_f} + \frac{\rho_{f1}\dot{V}_{c1}}{\rho_{f0}} + Q_{fu} + Q_{fc} = 0 \\ &\left(b\dot{e}_{v2} + \frac{\dot{p}_2}{M_b} \right) V_2 + \frac{V_{c2}\dot{p}_2}{K_f} + \frac{\rho_{f2}\dot{V}_{c2}}{\rho_{f0}} - Q_{fu} - Q_{fc} = 0 \end{aligned} \tag{11}$$

2.2 The Lattice Discrete Particle Model (LDPM) implementation

Following the discrete formulation of the FLE [32], by defining the discrete estimation of pore pressure flux in Eq. 7 as:

$$g_p = \mathbf{e} \cdot \mathbf{n} \left(p_2 - p_1 \right) / l \tag{12}$$

where p_1, p_2 are the values of fluid pressure at points N_1 and N_2, respectively, the governing equations for a FLE volume equivalent to Eqs. 11 can be rewritten as:

$$\begin{aligned} &\left(b\dot{e}_{v1} + \frac{\dot{p}_1}{M_b} \right) V_1 + \frac{V_{c1}\dot{p}_1}{K_f} + \frac{\rho_{f1}\dot{V}_{c1}}{\rho_{f0}} + \xi \frac{A}{l} \left(p_2 - p_1 \right) = 0 \\ &\left(b\dot{e}_{v2} + \frac{\dot{p}_2}{M_b} \right) V_2 + \frac{V_{c2}\dot{p}_2}{K_f} + \frac{\rho_{f2}\dot{V}_{c2}}{\rho_{f0}} - \xi \frac{A}{l} \left(p_2 - p_1 \right) = 0 \end{aligned} \tag{13}$$

where the effective permeability reads $\xi = \bar{\rho}_f \left(\kappa_0 + \kappa_c \right) / \left(\rho_{f0} \mu_f \right)$. The discrete-type governing equations in Eqs. 13 can then written in the matrix form, which reads:

$$\mathbf{M}\dot{\mathbf{p}} + \mathbf{K}\mathbf{p} + \mathbf{S} = \mathbf{0} \tag{14}$$

where,

$$\mathbf{M} = V \begin{bmatrix} g_1 C_1 & 0 \\ 0 & g_2 C_2 \end{bmatrix} \tag{15}$$

$$\mathbf{K} = \frac{A}{l} \begin{bmatrix} \xi & -\xi \\ -\xi & \xi \end{bmatrix} \tag{16}$$

$$\mathbf{S} = V \begin{bmatrix} g_1 S_1 & g_2 S_2 \end{bmatrix}^{\mathrm{T}} \tag{17}$$

$$\mathbf{p} = \begin{bmatrix} p_1 & p_2 \end{bmatrix}^{\mathrm{T}} \tag{18}$$

where $C_i = M_b^{-1} + V_{ci} \left(K_f V_i \right)^{-1}$ and $S_i = be_{vi} + \rho_{fi} V_c \left(\rho_{f0} V_i \right)^{-1}$. It is worth observing that, to reduce the memory requirements of the calculations, it is possible, without significant difference in the results, to substitute C_i and $S_i (i = 1, 2)$ with the volume averages $\bar{C} = g_1 C_1 + g_2 C_2$ and $\bar{S} = g_1 S_1 + g_2 S_2$.

In this project, the Backward Euler method was employed for time integration of the flow problem. Unlike continuous or other discrete models that utilize the same nodal sites for both mechanical and flow problems, dual lattice systems assign separate nodes for each system. This distinction introduces challenges when employing different solvers, such as explicit for mechanical computations and implicit for flow, since their time step sizes can vary significantly. In summary, the use of distinct meshes and different time scales further complicates the coupling process.

3 TWO-WAY COUPLING FRAMEWORK

The multiphysics problems can be solved in the so-called M-LDPM framework with the help of Interprocess Communication (IPC). Under this framework, each physical solver can be considered as an independent process. The periodic data communication between processes allows a sequential coupling mechanism. The spatial mappings and temporal synchronization between the two processes allow the coupling to run smoothly and robustly.

In the two-way coupling procedure, the algorithms are implemented through Abaqus user-defined elements VUEL (Explicit) for the LDPM and UEL (implicit) for the FLM. The two-way communication between LDPM and FLM during a single integration time step involves a sequence of steps executed in temporal order for each model. For LDPM, the process begins with updating the elements nodal positions and geometries. This is followed by exchanging data with the coupled analysis (FLM). Subsequently, strains and stresses are computed based on the constitutive models and multiphysics coupling mechanisms, finally internal forces are calculated in the LDPM elements.For the FLM, the workflow starts with updating element field variables, such as nodal pore pressures. Next, data is exchanged with the coupled analysis (LDPM). The tangential stiffness matrix (e.g., the Jacobian or AMATRX matrix) and the right-hand side vector (RHS vector) are then computed. Finally, an iterative process is performed to compute the increment until convergence is achieved, see Fig. 2.

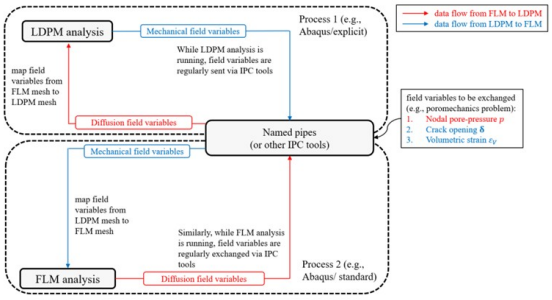

Figure 2: schematic diagram of M-LDPM two-way coupling procedure.

There are two typical coupling schemes: (1) parallel explicit coupling scheme (a.k.a. Jacobi scheme), both simulations are executed concurrently, exchanging fields to update the respective solutions at the next target time. This scheme is more efficient in the use of computing resources; less stable than the sequential scheme; (2) sequential explicit coupling scheme (a.k.a. Gauss-Seidel scheme), the simulations are executed in sequential order. One analysis leads while the other analysis lags the simulations. The parallel explicit coupling (Jacobi) scheme is used in this work.

In coupled processes with significantly different time scales, synchronization can be achieved using techniques like a time scaling factor, ktime, or subcycling. In subcycling, the implicit analysis with a larger time increment ramps loads over the coupling step, while the explicit analysis with a smaller time increment applies constant loads throughout the step. To address the large time increment discrepancies and optimize computational efficiency, this work employs both time scaling and subcycling approaches.

4 NUMERICAL RESULTS

The first numerical example is the classical one-dimension consolidation problem of Terzaghi [35]. A $0.5 \times 0.1 \times 0.1$ m^3 prism equivalent to infinite soil layer of thickness $L = 0.5$ m on a rigid impervious ground, is loaded by a stress $\sigma_z = t_z^*$ on the top surface at $z = 0$ under drained condition, the Dirichlet boundary conditions are $p = 0$ at $z = 0$ for the pore pressure,

and $u_z = 0$ at $z = L$, $u_x = u_y = 0$ at all lateral surfaces for the displacement. A schematic diagram of the numerical example is shown in Fig. 3a. LDPM and FLM meshes generated are shown in Fig. 4.

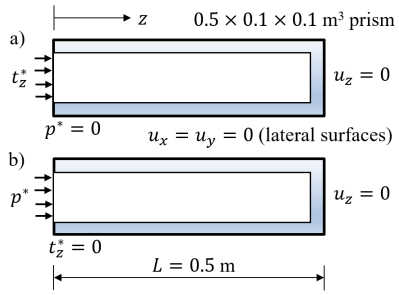

Figure 3: Two-way coupling verification 1: Terzaghi's 1D consolidation, simulation settings: a) loading by pressure, b) loading by traction.

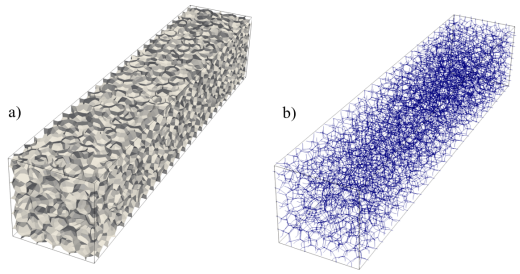

Figure 4: The LDPM tessellation of the prism's geometry for Terzaghi's 1D consolidation: a) LDPM mesh, b) FLM mesh.

The two-way coupling simulation results of loading mode 1 and 2 are presented in Figs. 6 and 7, respectively. Dimensionless fluid pressure p/p^*, as well as z displacement profiles u_z versus dimensionless coordinate $\chi = z/L$ at different time instants $t = 1/16t_{\text{sim}}$, $1/8t_{\text{sim}}$, $1/4t_{\text{sim}}$, $1/2t_{\text{sim}}$, and t_{sim}. It turned out that numerical model results agree well with the analytical solution, showing the validity of the two-way coupling framework on the simulation of poroelasticity problems.

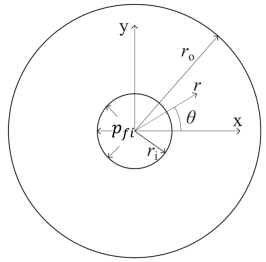

Figure 5: Radial expansion of a pressurized hollow cylinder, simulation settings adopted from [36].

The second numerical example is the potential fracture formation caused by continuous fluid injection into the hollow cylinder. The geometry of the hollow cylinder can be described by a $r-\theta-z$ cylindrical coordinate system with the inner surface at $r = r_i = 0.1$ m, the outer surface at $r = r_o = 0.725$ m, and the thickness $d = 0.1$ m, as shown in Fig. 5. The values of parameters used in this example are summarized in Tab. 1, note that we present results for low-permeability rocks with κ_0 =1.97E-20 m^2. For all fracture analyses, $\nu = 0.1$ was assumed.

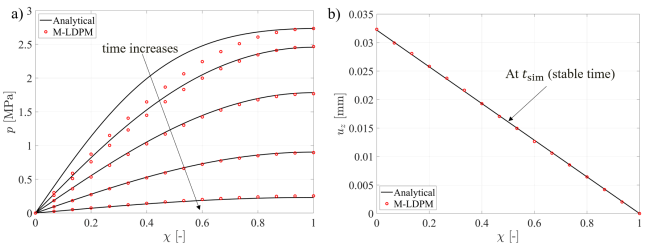

Figure 6: Terzhagi's consolidation, loading by traction: a) fluid pressure versus dimensionless coordinate $\chi = z/L$ at various times of simulation $t = 1/16t_{\text{sim}}, 1/8t_{\text{sim}}, 1/4t_{\text{sim}}, 1/2t_{\text{sim}}, t_{\text{sim}}$, and b) z displacement profiles versus dimensionless coordinate $\chi = z/L$ at t_{sim}.

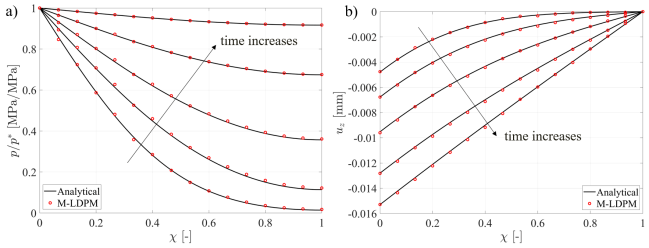

Figure 7: Terzhagi's consolidation, loading by fluid pressure: a) dimensionless fluid pressure p/p^* versus dimensionless coordinate $\chi = z/L$, and b) z displacement profiles u_z versus dimensionless coordinate $\chi = z/L$ at various times of simulation $t = 1/16t_{\text{sim}}, 1/8t_{\text{sim}}, 1/4t_{\text{sim}}, 1/2t_{\text{sim}}, t_{\text{sim}}$.

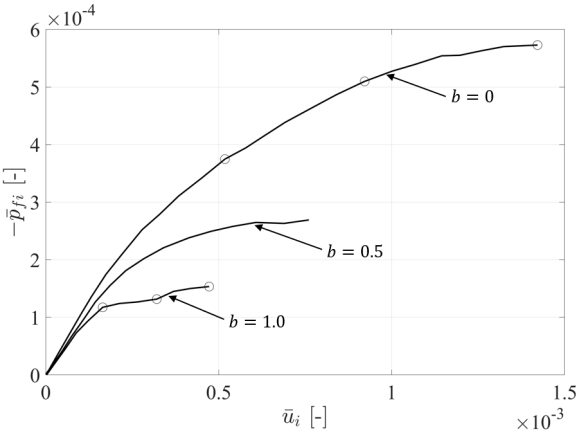

Figure 8: M-LDPM simulations of hydraulic fracturing of a pressurized hollow cylinder, normalized pressure $\bar{p}_{fi}$ versus normalized radial displacement $\bar{u}$ at the inner boundary at $r = r_i$. The circles indicate moments at which the crack patterns are shown in Figs. 9 and 10 for $b = 0$ and 1, respectively

Table 1: Input relevant parameters for two-way coupling simulations of hydraulic fracturing of a pressurized hollow cylinder

Description	Symbol [unit]	Value
Density of fluid	ρ_f [kg/m^3]	1.0E+03
Dynamic viscosity of fluid	μ_f [Pa.s]	8.9E-04
Bulk modulus of fluid	K_f [Pa]	2.15E+09
Intrinsic permeability	κ_0 [m^2]	1.97E-20
Biot modulus	M_b [Pa]	6.1728E+10
Biot coefficient	b [-]	0/0.5/1.0
Reference pressure	p_0 [Pa]	0.0
Density of solid	ρ_s [kg/m^3]	2.46E+03
Mesoscopic normal modulus of solid	E_0 [Pa]	4.648E+10
Mesoscopic normal-to-shear coefficient of solid	α [-]	0.5455
Mesoscopic tensile strength of solid	σ_t [Pa]	4.648E+06
Mesoscopic tensile characteristic length of solid	l_t [m]	0.2
Mesoscopic normal-to-shear strength ratio of solid	$r_s t$ [-]	4.1
Mesoscopic softening exponent of solid	n_t [-]	0.2
Mesoscopic compressive yielding stress of solid	σ_{c0} [Pa]	1E+08
Mesoscopic initial internal friction coefficient of solid	μ_0 [-]	0.2
Mesoscopic asymptotic internal friction coefficient of solid	μ_∞ [-]	0.0
Mesoscopic transitional normal stress of solid	σ_{N0} [Pa]	6E+08
Mesoscopic softening exponent of solid	H_0 [-]	0.2
Time scaling factor	k_{time} [-]	9.0E+06
Total simulation time	t_{sim} [s]	5E-02

The simulation results until the divergence of the solver due to the fracturing are presented in Fig. 8 in the form of normalized pressure $\bar{p}_{fi}$ versus normalized radial displacement $\bar{u}$ at the inner boundary for $b = 0$, 0.5 and 1. It can be observed that, Biot's coefficient has a strong influence on pressure–displacement curves in Fig. 8.

The circles in Fig. 8 indicate the moments at which the crack patterns are presented in Figs. 9 and 10 for $b = 0$ and $b = 1$, respectively. According to Figs. 9 and 10, the crack patterns change with Biot coefficient obviously: there is more diffused microcracking appearing at the critical pressure around the central hole for low Biot coefficients. This is due to different pressure magnitudes sustained by models with different Biot coefficients. When comparing cracking at the same pressure level, higher Biot coefficients result in more diffused cracking since fluid pressure reduces both radial and circumferential compressive stresses in the solid. The critical pressure for larger Biot coefficients is substantially lower.

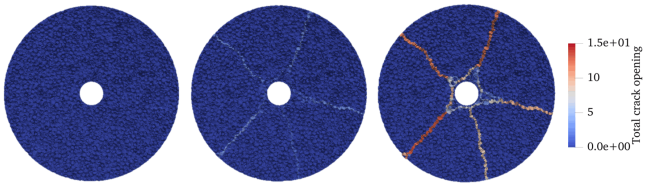

Figure 9: Crack patterns (crack opening contours) for uncoupled condition ($b = 0$) at three moments shown in Fig. 8.

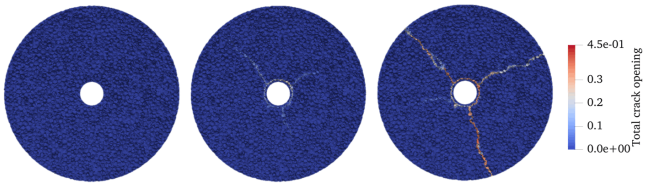

Figure 10: Crack patterns (crack opening contours) for $b = 1.0$ at three moments shown in Fig. 8.

5 CONCLUSION

This study presents a comprehensive Multiphysics-Lattice Discrete Particle Model (M-LDPM) framework designed for coupled fracture-poroflow problems in saturated environments. It integrates dual lattice systems: the LDPM tessellation for discrete particle interactions and the Flow Lattice Element (FLE) network for fluid flow simulations. The M-LDPM framework is implemented using Abaqus user element subroutines, with data communication between solvers facilitated by Interprocess Communication (IPC). Validation of the M-LDPM framework is performed through comparative analyses with analytical solutions of classical poromechanics benchmarks, demonstrating the framework's ability to accurately simulate both one-way and two-way coupling mechanisms with high fidelity. The M-LDPM results are align well with analytical solutions across varying Biot coefficients, and the framework effectively captures hydraulic fracturing, illustrating the interaction between crack propagation and fluid flow.

References

[1] P. A. Witherspoon, J. S. Wang, K. Iwai, and J. E. Gale. "Validity of cubic law for fluid flow in a deformable rock fracture". In: *Water resources research* 16.6 (1980), pp. 1016–1024.

[2] R. W. Zimmerman and G. S. Bodvarsson. "Hydraulic conductivity of rock fractures". In: *Transport in porous media* 23 (1996), pp. 1–30.

[3] I. Yeo, M. De Freitas, and R. Zimmerman. "Effect of shear displacement on the aperture and permeability of a rock fracture". In: *International journal of rock mechanics and mining sciences* 35.8 (1998), pp. 1051–1070.

[4] R. L. Detwiler. "Permeability alteration due to mineral dissolution in partially saturated fractures". In: *Journal of Geophysical Research: Solid Earth* 115.B9 (2010).

[5] J. E. Elkhoury, P. Ameli, and R. L. Detwiler. "Dissolution and deformation in fractured carbonates caused by flow of CO2-rich brine under reservoir conditions". In: *International Journal of Greenhouse Gas Control* 16 (2013), S203–S215.

[6] J. Rutqvist, J. Birkholzer, and C.-F. Tsang. "Coupled reservoir–geomechanical analysis of the potential for tensile and shear failure associated with CO2 injection in multilayered reservoir–caprock systems". In: *International Journal of Rock Mechanics and Mining Sciences* 45.2 (2008), pp. 132–143.

[7] M. Gutierrez, L. Øino, and R. Nygaard. "Stress-dependent permeability of a demineralised fracture in shale". In: *Marine and Petroleum Geology* 17.8 (2000), pp. 895–907.

[8] C. A. Davy, F. Skoczylas, J.-D. Barnichon, and P. Lebon. "Permeability of macro-cracked argillite under confinement: gas and water testing". In: *Physics and Chemistry of the Earth, Parts A/B/C* 32.8-14 (2007), pp. 667–680.

[9] Y. Cho, O. G. Apaydin, and E. Ozkan. "Pressure-dependent natural-fracture permeability in shale and its effect on shale-gas well production". In: *SPE Reservoir Evaluation & Engineering* 16.02 (2013), pp. 216–228.

[10] V. Luchnikov, N. Medvedev, L. Oger, and J.-P. Troadec. "Voronoi-Delaunay analysis of voids in systems of nonspherical particles". In: *Physical review E* 59.6 (1999), p. 7205.

[11] W. Brostow, M. Chybicki, R. Laskowski, and J. Rybicki. "Voronoi polyhedra and Delaunay simplexes in the structural analysis of molecular-dynamics-simulated materials". In: *Physical Review B* 57.21 (1998), p. 13448.

[12] M. G. Alinchenko, A. V. Anikeenko, N. N. Medvedev, V. P. Voloshin, M. Mezei, and P. Jedlovszky. "Morphology of voids in molecular systems. A Voronoi- Delaunay analysis of a simulated DMPC membrane". In: *The Journal of Physical Chemistry B* 108.49 (2004), pp. 19056–19067.

[13] V. P. Voloshin, A. V. Kim, N. N. Medvedev, R. Winter, and A. Geiger. "Calculation of the volumetric characteristics of biomacromolecules in solution by the Voronoi–Delaunay technique". In: *Biophysical Chemistry* 192 (2014), pp. 1–9.

[14] C. L. Palagi and K. Aziz. "Use of Voronoi grid in reservoir simulation". In: *SPE Advanced Technology Series* 2.02 (1994), pp. 69–77.

[15] L. Hashemi Beni, M. A. Mostafavi, J. Pouliot, and M. Gavrilova. "Toward 3D spatial dynamic field simulation within GIS using kinetic Voronoi diagram and Delaunay tetrahedralization". In: *International Journal of Geographical Information Science* 25.1 (2011), pp. 25–50.

[16] A. V. Anikeenko, M. Alinchenko, V. Voloshin, N. N. Medvedev, M. L. Gavrilova, and P. Jedlovszky. "Implementation of the Voronoi-Delaunay method for analysis of intermolecular voids". In: *Computational Science and Its Applications–ICCSA 2004: International Conference, Assisi, Italy, May 14-17, 2004, Proceedings, Part III 4*. Springer. 2004, pp. 217–226.

[17] P. Grassl. "A lattice approach to model flow in cracked concrete". In: *Cement and Concrete Composites* 31.7 (2009), pp. 454–460.

[18] P. Grassl and J. Bolander. "Three-dimensional network model for coupling of fracture and mass transport in quasi-brittle geomaterials". In: *Materials* 9.9 (2016), p. 782.

[19] C. Fahy, S. J. Wheeler, D. Gallipoli, and P. Grassl. "Corrosion induced cracking modelled by a coupled transport-structural approach". In: *Cement and Concrete Research* 94 (2017), pp. 24–35.

[20] O. I. Ulven and W. Sun. "Capturing the two-way hydromechanical coupling effect on fluid-driven fracture in a dual-graph lattice beam model". In: *International Journal for Numerical and Analytical Methods in Geomechanics* 42.5 (2018), pp. 736–767.

[21] I. Athanasiadis, S. J. Wheeler, and P. Grassl. "Hydro-mechanical network modelling of particulate composites". In: *International Journal of Solids and Structures* 130 (2018), pp. 49–60.

[22] D. Asahina, P. Pan, K. Tsusaka, M. Takeda, and J. E. Bolander. "Simulating hydraulic fracturing processes in laboratory-scale geological media using three-dimensional TOUGH-RBSN". In: *Journal of Rock Mechanics and Geotechnical Engineering* 10.6 (2018), pp. 1102–1111.

[23] W. Li, X. Zhou, J. W. Carey, L. P. Frash, and G. Cusatis. "Multiphysics lattice discrete particle modeling (M-LDPM) for the simulation of shale fracture permeability". In: *Rock Mechanics and Rock Engineering* 51 (2018), pp. 3963–3981.

[24] L. Shen, W. Li, X. Zhou, J. Feng, G. Di Luzio, Q. Ren, and G. Cusatis. "Multiphysics Lattice Discrete Particle Model for the simulation of concrete thermal spalling". In: *Cement and Concrete Composites* 106 (2020), p. 103457.

[25] L. Shen, H. Zhang, G. Di Luzio, H. Yin, L. Yang, and G. Cusatis. "Mesoscopic discrete modeling of multiaxial load-induced thermal strain of concrete at high temperature". In: *Interna-*

tional Journal of Mechanical Sciences 232 (2022), p. 107613.

[26] L. Yang, M. Pathirage, H. Su, M. Alnaggar, G. Di Luzio, and G. Cusatis. "Computational modeling of temperature and relative humidity effects on concrete expansion due to alkali–silica reaction". In: *Cement and Concrete Composites* 124 (2021), p. 104237.

[27] L. Yang, K. Li, X. Hu, Z. Peng, Q.-f. Liu, and C. Shi. "Mesoscopic discrete modeling of compression and fracture behavior of concrete: Effects of aggregate size distribution and interface transition zone". In: *Cement and Concrete Composites* 147 (2024), p. 105411.

[28] G. Cusatis, D. Pelessone, and A. Mencarelli. "Lattice Discrete Particle Model (LDPM) for Concrete failure Behavior of Concrete. I: Theory". In: *Cement and Concrete Composites* 33.9 (2011), pp. 881–890.

[29] G. Cusatis, A. Mencarelli, D. Pelessone, and J. Baylot. "Lattice Discrete Particle Model (LDPM) for Failure Behavior of Concrete. II: Calibration and Validation". In: *Cement and Concrete Composites* 33.9 (2011), pp. 891–905.

[30] E. Lale, J. Eliáš, K. Yu, M. Troemner, M. Středulová, J. Khoury, T. Xue, I. Koutromanos, A. Fascetti, M. Alnaggar, B. Ayhan, B. Chen, G. Di Luzio, Y. Lyu, M. Pathirage, G. Pijaudier-Cabot, L. Shen, A. Tasora, L. Yang, J. Zhong, and G. Cusatis. "Lattice Discrete Particle Model (LDPM): Comparison of Various Time Integration Solvers and Implementations". In: *Computer Physics Communications* ().

[31] M. A. Biot. "General Theory of Three-Dimensional Consolidation". In: *Journal of Applied Physics* 12.2 (1941), pp. 155–164.

[32] H. Yin, A. Cibelli, S.-A. Brown, L. Yang, L. Shen, M. Alnaggar, G. Cusatis, and G. Di Luzio. "Flow Lattice Model for the simulation of chemistry dependent transport phenomena in cementitious materials". In: *European Journal of Environmental and Civil Engineering* (2023), pp. 1–25.

[33] J. R. Rice and M. P. Cleary. "Some basic stress diffusion solutions for fluid-saturated elastic porous media with compressible constituents". In: *Reviews of Geophysics* 14.2 (1976), pp. 227–241.

[34] B. S. Massey and J. Ward-Smith. *Mechanics of fluids*. Vol. 1. Crc Press, 1998.

[35] K. von Terzaghi. "Die Berechnung der Durchassigkeitsziffer des Tones aus dem Verlauf der hydrodynamischen Spannungs. erscheinungen". In: *Sitzungsber. Akad. Wiss. Math. Naturwiss. Kl. Abt. 2A* 132 (1923), pp. 105–124.

[36] P. Grassl, C. Fahy, D. Gallipoli, and S. J. Wheeler. "On a 2D hydro-mechanical lattice approach for modelling hydraulic fracture". In: *Journal of the Mechanics and Physics of Solids* 75 (2015), pp. 104–118.